

Measurement of the sixth-order cumulant of net-proton multiplicity distributions in Au+Au collisions at $\sqrt{s_{NN}} = 27, 54.4, \text{ and } 200 \text{ GeV}$ at RHIC

M. S. Abdallah,⁵ J. Adam,⁶ L. Adamczyk,² J. R. Adams,³⁹ J. K. Adkins,³⁰ G. Agakishiev,²⁸ I. Aggarwal,⁴¹ M. M. Aggarwal,⁴¹ Z. Ahammed,⁶⁰ I. Alekseev,^{3,35} D. M. Anderson,⁵⁵ A. Aparin,²⁸ E. C. Aschenauer,⁶ M. U. Ashraf,¹¹ F. G. Atetalla,²⁹ A. Attri,⁴¹ G. S. Averichev,²⁸ V. Bairathi,⁵³ W. Baker,¹⁰ J. G. Ball Cap,²⁰ K. Barish,¹⁰ A. Behera,⁵² R. Bellwied,²⁰ P. Bhagat,²⁷ A. Bhasin,²⁷ J. Bielcik,¹⁴ J. Bielcikova,³⁸ I. G. Bordyuzhin,³ J. D. Brandenburg,⁶ A. V. Brandin,³⁵ I. Bunzarov,²⁸ J. Butterworth,⁴⁵ X. Z. Cai,⁵⁰ H. Caines,⁶³ M. Calderón de la Barca Sánchez,⁸ D. Cebra,⁸ I. Chakaberia,^{31,6} P. Chaloupka,¹⁴ B. K. Chan,⁹ F-H. Chang,³⁷ Z. Chang,⁶ N. Chankova-Bunzarova,²⁸ A. Chatterjee,¹¹ S. Chattopadhyay,⁶⁰ D. Chen,¹⁰ J. Chen,⁴⁹ J. H. Chen,¹⁸ X. Chen,⁴⁸ Z. Chen,⁴⁹ J. Cheng,⁵⁷ M. Chevalier,¹⁰ S. Choudhury,¹⁸ W. Christie,⁶ X. Chu,⁶ H. J. Crawford,⁷ M. Csanád,¹⁶ M. Daugherty,¹ T. G. Dedovich,²⁸ I. M. Deppner,¹⁹ A. A. Derevschikov,⁴³ A. Dhamija,⁴¹ L. Di Carlo,⁶² L. Didenko,⁶ X. Dong,³¹ J. L. Drachenberg,¹ E. Duckworth,²⁹ J. C. Dunlop,⁶ N. Elsey,⁶² J. Engelage,⁷ G. Eppley,⁴⁵ S. Esumi,⁵⁸ O. Evdokimov,¹² A. Ewigleben,³² O. Eyster,⁶ R. Fatemi,³⁰ F. M. Fawzi,⁵ S. Fazio,⁶ P. Federic,³⁸ J. Fedorisin,²⁸ C. J. Feng,³⁷ Y. Feng,⁴⁴ P. Filip,²⁸ E. Finch,⁵¹ Y. Fisyak,⁶ A. Francisco,⁶³ C. Fu,¹¹ L. Fulek,² C. A. Gagliardi,⁵⁵ T. Galatyuk,¹⁵ F. Geurts,⁴⁵ N. Ghimire,⁵⁴ A. Gibson,⁵⁹ K. Gopal,²³ X. Gou,⁴⁹ D. Grosnick,⁵⁹ A. Gupta,²⁷ W. Guryon,⁶ A. I. Hamad,²⁹ A. Hamed,⁵ Y. Han,⁴⁵ S. Harabasz,¹⁵ M. D. Harasty,⁸ J. W. Harris,⁶³ H. Harrison,³⁰ S. He,¹¹ W. He,¹⁸ X. H. He,²⁶ Y. He,⁴⁹ S. Heppelmann,⁸ S. Heppelmann,⁴² N. Herrmann,¹⁹ E. Hoffman,²⁰ L. Holub,¹⁴ Y. Hu,¹⁸ H. Huang,³⁷ H. Z. Huang,⁹ S. L. Huang,⁵² T. Huang,³⁷ X. Huang,⁵⁷ Y. Huang,⁵⁷ T. J. Humanic,³⁹ G. Igo,^{9,*} D. Isenhower,¹ W. W. Jacobs,²⁵ C. Jena,²³ A. Jentsch,⁶ Y. Ji,³¹ J. Jia,^{6,52} K. Jiang,⁴⁸ X. Ju,⁴⁸ E. G. Judd,⁷ S. Kabana,⁵³ M. L. Kabir,¹⁰ S. Kagamaster,³² D. Kalinkin,^{25,6} K. Kang,⁵⁷ D. Kapukchyan,¹⁰ K. Kauder,⁶ H. W. Ke,⁶ D. Keane,²⁹ A. Kechechyan,²⁸ Y. V. Khyzhniak,³⁵ D. P. Kikola,⁶¹ C. Kim,¹⁰ B. Kimelman,⁸ D. Kincses,¹⁶ I. Kisel,¹⁷ A. Kiselev,⁶ A. G. Knospe,³² L. Kochenda,³⁵ L. K. Kosarzewski,¹⁴ L. Kramerik,¹⁴ P. Kravtsov,³⁵ L. Kumar,⁴¹ S. Kumar,²⁶ R. Kunnawalkam Elayavalli,⁶³ J. H. Kwasizur,²⁵ R. Lacey,⁵² S. Lan,¹¹ J. M. Landgraf,⁶ J. Lauret,⁶ A. Lebedev,⁶ R. Lednický,²⁸ J. H. Lee,⁶ Y. H. Leung,³¹ C. Li,⁴⁹ C. Li,⁴⁸ W. Li,⁴⁵ X. Li,⁴⁸ Y. Li,⁵⁷ X. Liang,¹⁰ Y. Liang,²⁹ R. Licenik,³⁸ T. Lin,⁵⁵ Y. Lin,¹¹ M. A. Lisa,³⁹ F. Liu,¹¹ H. Liu,²⁵ H. Liu,¹¹ P. Liu,⁵² T. Liu,⁶³ X. Liu,³⁹ Y. Liu,⁵⁵ Z. Liu,⁴⁸ T. Ljubicic,⁶ W. J. Llope,⁶² R. S. Longacre,⁶ E. Loyd,¹⁰ N. S. Lukow,⁵⁴ X. Luo,¹¹ L. Ma,¹⁸ R. Ma,⁶ Y. G. Ma,¹⁸ N. Magdy,¹² R. Majka,^{63,*} D. Mallick,³⁶ S. Margetis,²⁹ C. Markert,⁵⁶ H. S. Matis,³¹ J. A. Mazer,⁴⁶ N. G. Minaev,⁴³ S. Mioduszewski,⁵⁵ B. Mohanty,³⁶ M. M. Mondal,⁵² I. Mooney,⁶² D. A. Morozov,⁴³ A. Mukherjee,¹⁶ M. Nagy,¹⁶ J. D. Nam,⁵⁴ Md. Nasim,²² K. Nayak,¹¹ D. Neff,⁹ J. M. Nelson,⁷ D. B. Nemes,⁶³ M. Nie,⁴⁹ G. Nigmatkulov,³⁵ T. Niida,⁵⁸ R. Nishitani,⁵⁸ L. V. Nogach,⁴³ T. Nonaka,⁵⁸ A. S. Nunes,⁶ G. Odyniec,³¹ A. Ogawa,⁶ S. Oh,³¹ V. A. Okorokov,³⁵ B. S. Page,⁶ R. Pak,⁶ A. Pandav,³⁶ A. K. Pandey,⁵⁸ Y. Panebratsev,²⁸ P. Parfenov,³⁵ B. Pawlik,⁴⁰ D. Pawlowska,⁶¹ H. Pei,¹¹ C. Perkins,⁷ L. Pinsky,²⁰ R. L. Pintér,¹⁶ J. Pluta,⁶¹ B. R. Pokhrel,⁵⁴ G. Ponimatkin,³⁸ J. Porter,³¹ M. Posik,⁵⁴ V. Prozorova,¹⁴ N. K. Pruthi,⁴¹ M. Przybycien,² J. Putschke,⁶² H. Qiu,²⁶ A. Quintero,⁵⁴ C. Racz,¹⁰ S. K. Radhakrishnan,²⁹ N. Raha,⁶² R. L. Ray,⁵⁶ R. Reed,³² H. G. Ritter,³¹ M. Robotkova,³⁸ O. V. Rogachevskiy,²⁸ J. L. Romero,⁸ L. Ruan,⁶ J. Rusnak,³⁸ N. R. Sahoo,⁴⁹ H. Sako,⁵⁸ S. Salur,⁴⁶ J. Sandweiss,^{63,*} S. Sato,⁵⁸ W. B. Schmidke,⁶ N. Schmitz,³³ B. R. Schweid,⁵² F. Seck,¹⁵ J. Seger,¹³ M. Sergeeva,⁹ R. Seto,¹⁰ P. Seyboth,³³ N. Shah,²⁴ E. Shahaliev,²⁸ P. V. Shanmuganathan,⁶ M. Shao,⁴⁸ T. Shao,⁵⁰ A. I. Sheikh,²⁹ D. Shen,⁵⁰ S. S. Shi,¹¹ Y. Shi,⁴⁹ Q. Y. Shou,¹⁸ E. P. Sichtermann,³¹ R. Sikora,² M. Simko,³⁸ J. Singh,⁴¹ S. Singha,²⁶ M. J. Skoby,⁴⁴ N. Smirnov,⁶³ Y. Söhngen,¹⁹ W. Solyst,²⁵ P. Sorensen,⁶ H. M. Spinka,^{4,*} B. Srivastava,⁴⁴ T. D. S. Stanislaus,⁵⁹ M. Stefaniak,⁶¹ D. J. Stewart,⁶³ M. Strikhanov,³⁵ B. Stringfellow,⁴⁴ A. A. P. Suaide,⁴⁷ M. Sumera,³⁸ B. Summa,⁴² X. M. Sun,¹¹ X. Sun,¹² Y. Sun,⁴⁸ Y. Sun,²¹ B. Surrow,⁵⁴ D. N. Svirida,³ Z. W. Sweger,⁸ P. Szymanski,⁶¹ A. H. Tang,⁶ Z. Tang,⁴⁸ A. Taranenko,³⁵ T. Tarnowsky,³⁴ J. H. Thomas,³¹ A. R. Timmins,²⁰ D. Tlusty,¹³ T. Todoroki,⁵⁸ M. Tokarev,²⁸ C. A. Tomkiel,³² S. Trentalange,⁹ R. E. Tribble,⁵⁵ P. Tribedy,⁶ S. K. Tripathy,¹⁶ T. Truhlar,¹⁴ B. A. Trzeciak,¹⁴ O. D. Tsai,⁹ Z. Tu,⁶ T. Ullrich,⁶ D. G. Underwood,⁴ I. Upsal,^{49,6} G. Van Buren,⁶ J. Vanek,³⁸ A. N. Vasiliev,⁴³ I. Vassiliev,¹⁷ V. Verkest,⁶² F. Videbæk,⁶ S. Vokal,²⁸ S. A. Voloshin,⁶² F. Wang,⁴⁴ G. Wang,⁹ J. S. Wang,²¹ P. Wang,⁴⁸ Y. Wang,¹¹ Y. Wang,⁵⁷ Z. Wang,⁴⁹ J. C. Webb,⁶ P. C. Weidenkaff,¹⁹ L. Wen,⁹ G. D. Westfall,³⁴ H. Wieman,³¹ S. W. Wissink,²⁵ J. Wu,²⁶ Y. Wu,¹⁰ B. Xi,⁵⁰ Z. G. Xiao,⁵⁷ G. Xie,³¹ W. Xie,⁴⁴ H. Xu,²¹ N. Xu,³¹ Q. H. Xu,⁴⁹ Y. Xu,⁴⁹ Z. Xu,⁶ Z. Xu,⁹ C. Yang,⁴⁹ Q. Yang,⁴⁹ S. Yang,⁴⁵ Y. Yang,³⁷ Z. Ye,⁴⁵ Z. Ye,¹² L. Yi,⁴⁹ K. Yip,⁶ Y. Yu,⁴⁹ H. Zbroszczyk,⁶¹ W. Zha,⁴⁸ C. Zhang,⁵² D. Zhang,¹¹ J. Zhang,⁴⁹ S. Zhang,¹² S. Zhang,¹⁸ X. P. Zhang,⁵⁷ Y. Zhang,²⁶ Y. Zhang,⁴⁸ Y. Zhang,¹¹ Z. J. Zhang,³⁷ Z. Zhang,⁶ Z. Zhang,¹² J. Zhao,⁴⁴ C. Zhou,¹⁸ X. Zhu,⁵⁷ Z. Zhu,⁴⁹ M. Zurek,³¹ and M. Zyzak¹⁷

(STAR Collaboration)

¹Abilene Christian University, Abilene, Texas 79699

²AGH University of Science and Technology, FPACS, Cracow 30-059, Poland

³Alikhanov Institute for Theoretical and Experimental Physics NRC "Kurchatov Institute", Moscow 117218, Russia

⁴Argonne National Laboratory, Argonne, Illinois 60439

⁵American University of Cairo, New Cairo 11835, New Cairo, Egypt

- ⁶Brookhaven National Laboratory, Upton, New York 11973
⁷University of California, Berkeley, California 94720
⁸University of California, Davis, California 95616
⁹University of California, Los Angeles, California 90095
¹⁰University of California, Riverside, California 92521
¹¹Central China Normal University, Wuhan, Hubei 430079
¹²University of Illinois at Chicago, Chicago, Illinois 60607
¹³Creighton University, Omaha, Nebraska 68178
¹⁴Czech Technical University in Prague, FNSPE, Prague 115 19, Czech Republic
¹⁵Technische Universität Darmstadt, Darmstadt 64289, Germany
¹⁶ELTE Eötvös Loránd University, Budapest, Hungary H-1117
¹⁷Frankfurt Institute for Advanced Studies FIAS, Frankfurt 60438, Germany
¹⁸Fudan University, Shanghai, 200433
¹⁹University of Heidelberg, Heidelberg 69120, Germany
²⁰University of Houston, Houston, Texas 77204
²¹Huzhou University, Huzhou, Zhejiang 313000
²²Indian Institute of Science Education and Research (IISER), Berhampur 760010, India
²³Indian Institute of Science Education and Research (IISER) Tirupati, Tirupati 517507, India
²⁴Indian Institute Technology, Patna, Bihar 801106, India
²⁵Indiana University, Bloomington, Indiana 47408
²⁶Institute of Modern Physics, Chinese Academy of Sciences, Lanzhou, Gansu 730000
²⁷University of Jammu, Jammu 180001, India
²⁸Joint Institute for Nuclear Research, Dubna 141 980, Russia
²⁹Kent State University, Kent, Ohio 44242
³⁰University of Kentucky, Lexington, Kentucky 40506-0055
³¹Lawrence Berkeley National Laboratory, Berkeley, California 94720
³²Lehigh University, Bethlehem, Pennsylvania 18015
³³Max-Planck-Institut für Physik, Munich 80805, Germany
³⁴Michigan State University, East Lansing, Michigan 48824
³⁵National Research Nuclear University MEPhI, Moscow 115409, Russia
³⁶National Institute of Science Education and Research, HBNI, Jatni 752050, India
³⁷National Cheng Kung University, Tainan 70101
³⁸Nuclear Physics Institute of the CAS, Rez 250 68, Czech Republic
³⁹Ohio State University, Columbus, Ohio 43210
⁴⁰Institute of Nuclear Physics PAN, Cracow 31-342, Poland
⁴¹Panjab University, Chandigarh 160014, India
⁴²Pennsylvania State University, University Park, Pennsylvania 16802
⁴³NRC "Kurchatov Institute", Institute of High Energy Physics, Protvino 142281, Russia
⁴⁴Purdue University, West Lafayette, Indiana 47907
⁴⁵Rice University, Houston, Texas 77251
⁴⁶Rutgers University, Piscataway, New Jersey 08854
⁴⁷Universidade de São Paulo, São Paulo, Brazil 05314-970
⁴⁸University of Science and Technology of China, Hefei, Anhui 230026
⁴⁹Shandong University, Qingdao, Shandong 266237
⁵⁰Shanghai Institute of Applied Physics, Chinese Academy of Sciences, Shanghai 201800
⁵¹Southern Connecticut State University, New Haven, Connecticut 06515
⁵²State University of New York, Stony Brook, New York 11794
⁵³Instituto de Alta Investigación, Universidad de Tarapacá, Arica 1000000, Chile
⁵⁴Temple University, Philadelphia, Pennsylvania 19122
⁵⁵Texas A&M University, College Station, Texas 77843
⁵⁶University of Texas, Austin, Texas 78712
⁵⁷Tsinghua University, Beijing 100084
⁵⁸University of Tsukuba, Tsukuba, Ibaraki 305-8571, Japan
⁵⁹Valparaiso University, Valparaiso, Indiana 46383
⁶⁰Variable Energy Cyclotron Centre, Kolkata 700064, India
⁶¹Warsaw University of Technology, Warsaw 00-661, Poland
⁶²Wayne State University, Detroit, Michigan 48201
⁶³Yale University, New Haven, Connecticut 06520

According to first principle Lattice QCD calculations, the transition from quark-gluon plasma to hadronic matter is a smooth crossover in the region $\mu_B \leq T_c$. In this range the ratio, C_6/C_2 , of net-baryon distributions are predicted to be negative. In this paper, we report the first measurement of the midrapidity net-proton C_6/C_2 from 27, 54.4 and 200 GeV Au+Au collisions at RHIC. The dependence on collision centrality and kinematic acceptance in (p_T, y) are analyzed. While for 27 and 54.4 GeV collisions the C_6/C_2 values are close to zero within uncertainties, it is observed that for 200 GeV collisions, the C_6/C_2 ratio becomes progressively negative from peripheral to central collisions. Transport model calculations without critical dynamics predict mostly positive values except for the most central collisions within uncertainties. These observations seem to favor a smooth crossover in the high energy nuclear collisions at top RHIC energy.

One of the main goals of high-energy nuclear physics is to understand the phase diagram of the strongly interacting matter predicted by quantum chromo-dynamics (QCD), with respect to temperature (T) and baryon chemical potential (μ_B). At high T and/or μ_B , the strongly interacting matter called quark-gluon plasma (QGP) is predicted to exist, while the hadronic matter appears at low T [1–3]. The phase transition between QGP and hadronic matter at $\mu_B \approx 0$ was shown to be a smooth crossover, based on first-principle lattice QCD calculations [4]. At finite μ_B , on the other hand, the phase transition is predicted to be of the first order [5]. If this is true, a critical end point may also exist, which is the connecting point between crossover and the first-order phase transition [6].

Experimentally, the QCD phase diagram can be explored by measuring heavy-ion collisions at various collision energies. The beam energy scan (BES) program was carried out at the Relativistic Heavy-Ion Collider (RHIC), and data sets for Au+Au collisions at $\sqrt{s_{NN}} = 7.7, 11.5, 14.5, 19.6, 27, 39, 54.4, 62.4,$ and 200 GeV were collected by the STAR experiment. The r th-order cumulants (C_r) and their ratios up to the fourth-order of net-charge, net-proton, and net-kaon multiplicity distributions have been measured to search for the critical point [7–12]. In particular, the ratio C_4/C_2 of the net-proton multiplicity distributions with an extended p_T coverage shows a non-monotonic beam energy dependence in Au+Au central collisions [9]. This is qualitatively consistent with a theoretical model prediction which incorporates a critical point [13, 14]. Since the results are dominated by large statistical uncertainties at low collision energies, the beam energy scan phase II (BES-II) and the fixed-target programs are being performed to detect more definitive signatures of the critical point [15]. New findings on the QCD phase structure at large μ_B are thus expected in the near future from the BES-II program.

There is no direct experimental evidence of a smooth crossover at $\mu_B \approx 0$ MeV as predicted by the lattice QCD calculations. This can be studied by measuring the ratio of the sixth to second-order cumulant (C_6/C_2) of net-baryon and net-charge multiplicity distributions. According to the QCD model calculations, the C_6/C_2 values of net-baryon distributions become negative at $\sqrt{s_{NN}} \geq 60$ GeV if the freeze-out, where ratios of particle yields are fixed, occurs near the chiral crossover temperature [16], whereas the hadron resonance gas model calculations yield a positive sign for C_6/C_2 [17]. Recent model studies predict a negative sign of C_6/C_2 at $\sqrt{s_{NN}} \geq 7.7$ GeV within large uncertainties [18]. Furthermore, recent lattice QCD calculations also show a negative sign of the ratio of the sixth-order to the second-order baryon number susceptibilities, χ_6^B/χ_2^B , at the transition temperature for $\sqrt{s_{NN}} \geq 39$ GeV [17, 19]. The susceptibility ratio can be compared to a corresponding ratio of experimentally measured cumulants.

This Letter reports C_6/C_2 of event-by-event net-proton multiplicity ($N_p - N_{\bar{p}} = \Delta N_p$) distributions for Au+Au collisions at $\sqrt{s_{NN}} = 27, 54.4,$ and 200 GeV. These

three collision energies correspond to $\mu_B = 144, 83,$ and 28 MeV, respectively, for the most central collisions [20]. The data sets for $\sqrt{s_{NN}} = 54.4$ and 27 GeV were taken in 2017 and 2018. The data for 200 GeV were collected in 2010 and 2011. The numbers of events analyzed for 0-80% centrality at $\sqrt{s_{NN}} = 27, 54.4,$ and 200 GeV are around 280, 520, and 900 million, respectively. All data were taken with a minimum bias trigger, except for 0-10% centrality of 200 GeV data in 2010, which was taken with a special trigger with enhanced event samples for central collisions. All data were taken with the time projection chamber (TPC) and the time of flight (TOF) detector at the solenoid tracker at RHIC (STAR). Events occurring within $|\Delta Z| < 30$ cm from the center of the TPC along the beam line (Z -direction) are selected. The transverse positions of the collisions are required to be within $|\Delta R| < 2$ cm to reject interactions between the beam and the beam pipe [20]. Events from pileup, which is defined as the superposition of several single-collision events occurring within a small space and time interval, are rejected by cutting on the correlation between the charged particle multiplicity measured by the TPC and extrapolated tracks from the TPC to the hit positions in the TOF.

The collision centrality is defined using the charged particle multiplicities measured by the TPC in $|\eta| < 1.0$. Protons and antiprotons are excluded from the above centrality definition in order to minimize self-correlation effects [21]. Event-by-event numbers of protons and antiprotons are measured at midrapidity, $|y| < 0.5$, for the transverse momentum range $0.4 < p_T$ (GeV/c) < 2.0 . Protons and antiprotons at $0.4 < p_T$ (GeV/c) < 0.8 are identified using ionization energy loss distributions measured by the TPC (dE/dx), while at $0.8 < p_T$ (GeV/c) < 2.0 they are identified using the mass squared (m^2) distributions measured by the TOF as well. The lower limit of the p_T range is chosen to reject the secondary protons produced by interactions with the beam pipe. Requiring the distance of closest approach to be less than 1 cm with respect to the collision vertex suppresses the effect from the contribution of weak decay daughter protons. Weak decay protons which passed this cut are all included in the analysis. Up to the fourth order, the effect of the decay is found to be small [22]. The purity of protons and antiprotons in the analyzed acceptance is higher than 95% for $\sqrt{s_{NN}} = 27, 54.4,$ and 200 GeV.

Event-by-event net-proton number (ΔN_p) distributions for Au+Au collisions at $\sqrt{s_{NN}} = 27, 54.4,$ and 200 GeV for 0-10% and 30-40% centralities are shown in Fig. 1. The plotted distributions are normalized by the corresponding total number of events and are not corrected for detector efficiencies. The distributions for 0-10% are broader than for 30-40% as more protons and antiprotons are produced in central collisions. The shape of the distribution is characterized by various orders of cumulants [23]. Definitions and formulas for cumulant calculations can be found in the Supplemental Material. Cumulants are extensive variables proportional to the volume of the collision system [23]. This undesired volume effect is canceled by taking the ratio of different order cumulants. Then the C_6/C_2 value can be compared with the ratio of baryon number susceptibilities (χ_6^B/χ_2^B) from lattice QCD calculations, keeping in mind

* Deceased

the difference between net-baryon from theory calculations and net-proton from the data within the limited experimental acceptance. When multiplicities of protons and antiprotons follow Poisson distributions, the resulting net-proton distribution is called a Skellam distribution. The odd-order and even-order cumulants of the Skellam distribution are expressed by the difference and sum of the mean values (C_1) of the Poisson distributions, respectively. Hence, $C_6/C_2 = 1$ for the Skellam distribution. The Skellam distributions determined from C_1 of protons and antiprotons for each collision energy and centrality are shown by dashed lines in Fig. 1. According to the ratio of data to the Skellam expectations, shown in the lower part of Fig. 1, deviations from the Skellam distributions are seen especially at the tails of the distribution.

It is known that the statistical uncertainties on higher-order cumulants become larger for broader distributions [21]. A model study indicates that higher-order cumulants suffer from larger statistical uncertainties. The effect increases with increasing order of the cumulant [24]. Statistical uncertainties also depend on the detector efficiencies. A lower efficiency gives larger statistical errors for cumulants after efficiency corrections.

A centrality bin width correction is applied for each centrality bin to suppress the effect from the initial volume fluctuations [21, 25, 26]. Statistical uncertainties are calculated using a bootstrap method [21, 27].

All results of C_6/C_2 presented in this Letter are corrected for the detector efficiency assuming that the detector efficiencies follow the binomial distribution [24, 28–34]. Non-binomial efficiencies [35] are also studied through detector simulations in the STAR environment. Cumulants are corrected for non-binomial efficiencies using the unfolding and moment expansion approaches [36, 37]. Results up to the sixth-order cumulant for Au+Au central collisions at $\sqrt{s_{NN}} = 200$ GeV are presented in the Supplemental Material. It is concluded that the results corrected for non-binomial efficiencies are consistent with the results from the binomial efficiency correction within statistical uncertainties.

Systematic uncertainties are estimated by changing the following variables used to select protons and antiprotons: the distance of closest approach to the primary collision vertex and number of hits in the TPC to reconstruct tracks for the track quality cut, dE/dx , and m^2 selections for (anti)proton identification criteria. A Barlow check is done to remove the statistical effects from being counted as part of systematic uncertainties [38]. The contribution from track quality cuts is dominant for central collisions. The systematic uncertainties from each source go down below 10% in peripheral collisions. The uncertainties for each source are then added in quadrature. The total systematic uncertainties are 87%, 70%, and 37% at 27, 54.4, and 200 GeV, respectively, for 0-10% central collisions, and the corresponding totals decrease down to a few percent in peripheral collisions.

Figure 2 shows the net-proton C_6/C_2 for Au+Au collisions for 0-10% and 30-40% centralities at $\sqrt{s_{NN}} = 27, 54.4,$ and 200 GeV as a function of rapidity and p_T acceptance. The values of C_6/C_2 approach the Skellam expectation, $C_6/C_2 = 1$, with narrow acceptance in p_T and rapidity. The reason is that multiplicity distribu-

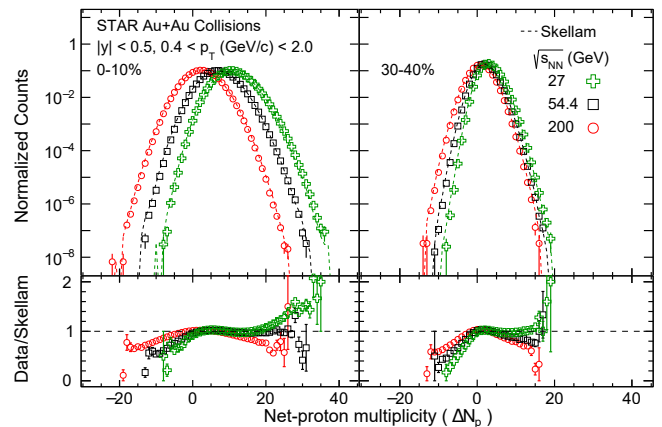


FIG. 1. Event by event net-proton multiplicity, ΔN_p , distributions for Au+Au collisions at $\sqrt{s_{NN}} = 27, 54.4,$ and 200 GeV in 0-10%(left) and 30-40%(right) centralities at midrapidity ($|y| < 0.5$) for the transverse momentum range of $0.4 < p_T$ (GeV/c) < 2.0 . These distributions are normalized by the corresponding numbers of events and are not corrected for detector efficiencies. Statistical uncertainties are shown as vertical lines. The dashed lines show the Skellam distributions for each collision energy and centrality. The bottom panels show the ratio of the data to the Skellam expectations.

tions of protons and antiprotons are close to the Poisson distribution because of lower particle multiplicity and thus less correlations, and therefore the observed C_6/C_2 is dominated by statistical fluctuations. The fraction of measured protons to total protons integrated in whole p_T region is 33% for $0.4 < p_T$ (GeV/c) < 0.8 and 86% for $0.4 < p_T$ (GeV/c) < 2.0 at 200 GeV. Although the C_6/C_2 values at the smallest acceptance of $|y| < 0.1$ or $0.4 < p_T$ (GeV/c) < 0.8 in Fig. 2 are still smaller than unity, we have checked that the results are consistent with unity with further narrowed acceptance. The C_6/C_2 values for 0-10% centrality decrease as the acceptance is increased at 27 GeV, while C_6/C_2 is nearly constant for 54.4 and 200 GeV within uncertainties. On the other hand, the results for 30-40% centrality show a strong decrease with increasing acceptance at 200 GeV and are almost flat for 27 and 54.4 GeV. Results from the transport model UrQMD [39], in which hadronic interactions are dominant and there is no phase transition implemented, are shown by shaded and hatched-bands in Fig. 2. The event statistics used in the UrQMD calculations are 215, 100, and 95 million for 27, 54.4, and 200 GeV minimum bias Au+Au collisions, respectively. All experimental cuts in terms of the collision centrality, rapidity, and transverse momentum acceptance are applied in the calculations. The C_6/C_2 values from UrQMD are flat as a function of rapidity and p_T acceptance at 27 and 200 GeV, while the sign changes for central collisions at 54.4 GeV albeit with large uncertainties. Note that the thermal blurring in rapidity for conserved charges is discussed in Ref. [40]. More studies are necessary in order to understand the rapidity dependence as a function of collision energies.

In Fig. 3, the centrality dependence of the net-proton C_6/C_2 at midrapidity is shown for all three collision energies. The data with the largest number of participant nucleons (N_{part}) corresponds to the top 0-10% central

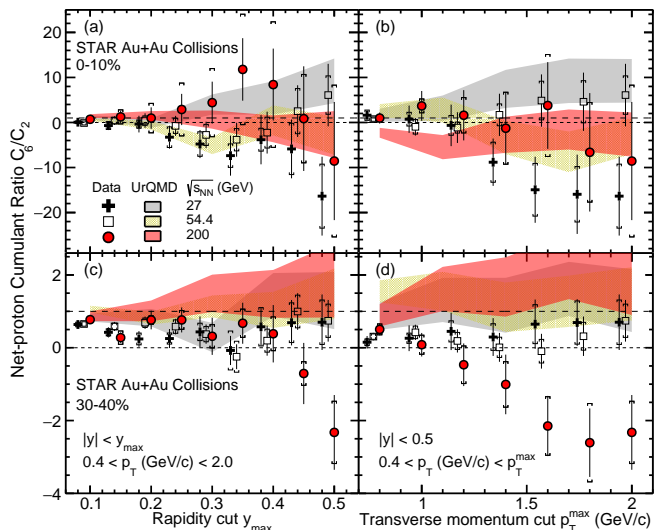


FIG. 2. Net-proton C_6/C_2 as a function of rapidity (left) and transverse momentum acceptance (right) from $\sqrt{s_{\text{NN}}} = 27$ (crosses), 54.4 (open squares), and 200 GeV (filled circles) Au+Au collisions. The upper and lower plots are for 0-10% and 30-40% centralities, respectively. The error bars are statistical and caps are systematic errors. Points for different beam energies are staggered horizontally to improve clarity. UrQMD transport model results are shown as shaded and hatched bands. The Skellam expectation ($C_6/C_2 = 1$) is shown as long-dashed lines.

collisions and the rest of the points are for 10-20%, 20-30%, 30-40%,... , and 70-80% centralities. For 200 GeV collisions (filled circles), C_6/C_2 values are approaching the Skellam expectation ($C_6/C_2 = 1$) from central to peripheral collisions. The C_6/C_2 values then start to be negative from 50-60% centrality, and stay negative systematically in central collisions within large uncertainties. Most C_6/C_2 measurements at 27 and 54.4 GeV are consistent with zero within uncertainties. We find that the C_6/C_2 values are negative within 1.7 sigma at 200 GeV 30-40% centrality with statistical and systematic uncertainties added in quadrature.

QCD-inspired model calculations [16] show that at vanishing baryon chemical potential, the crossover transition from the QGP to hadronic phase and its remnants will affect higher-order cumulant ratios. The model further suggests that the value of C_6/C_2 of the net-baryon distribution should be positive and negative for the emerging medium from hadronic and QGP phases, respectively. All of the results from the UrQMD calculations are consistent with the Skellam expectation ($C_6/C_2 = 1$) within large statistical fluctuations towards more central collisions. Overall, the UrQMD calculations of the net-proton C_6/C_2 reproduce, within errors, the measured centrality dependence for 27 and 54.4 GeV Au+Au collisions. Experimental results for 200 GeV are below UrQMD calculations systematically from peripheral to central collisions.

First-principle lattice QCD calculations offer accurate information on the properties of a thermalized system with zero baryon chemical potential. For example, see Ref. [4]. By a Taylor expansion at small μ_B , one could extend the predictions to finite values of the baryon chemi-

cal potential. The lattice calculations with a temperature of 160 MeV and baryon chemical potential up to $\mu_B \sim 110$ MeV are shown as the blue band in Fig. 3 [17, 19]. Lattice calculations also indicate that in the region of $\mu_B/T < 1$, the transition from QGP to hadronic matter is a smooth crossover [17]. The μ_B/T ratios are approximately 0.17, 0.55, and 0.93 for central Au+Au collisions at $\sqrt{s_{\text{NN}}} = 200, 54,$ and 27 GeV, respectively. Please note there are caveats when comparing experimental data with lattice calculations. While the current experimental data are midrapidity net-proton distributions from the kinematic region of $|y| < 0.5$ and $0.4 < p_T$ (GeV/c) < 2.0 , the lattice results are for net-baryons and do not incorporate any of the experimental kinematic cuts [28]. It is also known that the cumulants are affected by both baryon number conservation and baryon stopping [41–44] which are expected to be more significant towards lower collision energies [45, 46]. Both effects are present in the results presented here. In addition, the lattice simulates a thermalized system but without other dynamics such as collective expansion in high-energy nuclear collisions. These differences between experiments and lattice calculations need to be carefully handled in the future for a quantitative comparison. With these caveats in mind, the trend observed in Au+Au collisions at 200 GeV that C_6/C_2 becomes negative with increasing centrality is potentially consistent with the smooth crossover scenario. Higher statistics data sets are necessary in order to establish trend in the finite μ_B range.

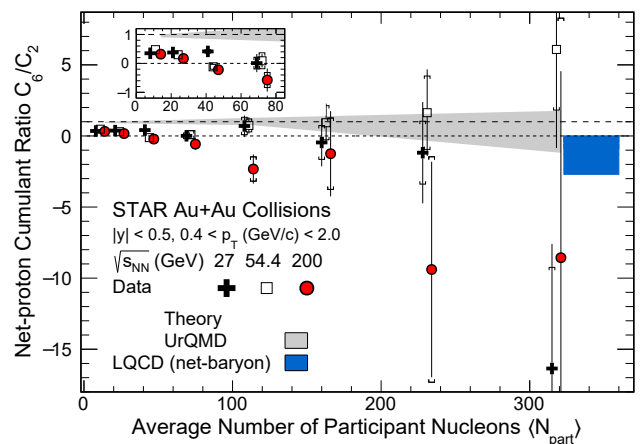


FIG. 3. Collision centrality dependence of net-proton C_6/C_2 in Au+Au collisions for $\sqrt{s_{\text{NN}}} = 27, 54.4,$ and 200 GeV within $|y| < 0.5$ and $0.4 < p_T$ (GeV/c) < 2.0 . The error bars are statistical and caps are systematic errors. Points for different beam energies are staggered horizontally to improve clarity. A shaded band shows the results from UrQMD model calculations. UrQMD calculations from the above three collision energies are consistent among them so they are merged in order to reduce statistical fluctuations. Details on these calculations can be found in the Supplemental Material. The lattice QCD calculations on net-baryon number fluctuations [17, 19] for $T = 160$ MeV and $\mu_B < 110$ MeV. are shown as a blue band at $\langle N_{\text{part}} \rangle \approx 340$. The inset shows the expanded region of 40-80% centrality.

In summary, we report the first measurements of the net-proton higher-order cumulant ratio C_6/C_2 from 27, 54.4 and 200 GeV Au+Au collisions measured by the

STAR detector at RHIC. The data is taken from the kinematic region ($|y| < 0.5$ and $0.4 < p_T$ (GeV/c) < 2.0). Data from 200 GeV collisions are found to be negative progressively in more central collisions within the maximum acceptance, while the ratios from 27 and 54.4 GeV collisions are found to be close to zero within uncertainties. Without critical dynamics, the transport model UrQMD calculations predict the ratio C_6/C_2 around a statistical baseline in all cases. Lattice QCD calculations, with $T = 160$ MeV and $\mu_B = 0-110$ MeV, predict the negative value of $C_6/C_2 \sim -1.5$, which is qualitatively consistent with the experimental results of central Au+Au collisions at top RHIC energies. These new measurements are statistics limited and seem to favor a smooth crossover for the QGP-hadronic matter transition. Future measurements with high statistics will provide more detailed information about the phase structure at the low baryon density region.

We thank the RHIC Operations Group and RCF at BNL, the NERSC Center at LBNL, and the Open Science Grid consortium for providing resources and support. This work was supported in part by the Office

of Nuclear Physics within the U.S. DOE Office of Science, the U.S. National Science Foundation, the Ministry of Education and Science of the Russian Federation, National Natural Science Foundation of China, Chinese Academy of Science, the Ministry of Science and Technology of China and the Chinese Ministry of Education, the Higher Education Sprout Project by Ministry of Education at NCKU, the National Research Foundation of Korea, Czech Science Foundation and Ministry of Education, Youth and Sports of the Czech Republic, Hungarian National Research, Development and Innovation Office, New National Excellency Programme of the Hungarian Ministry of Human Capacities, Department of Atomic Energy and Department of Science and Technology of the Government of India, the National Science Centre of Poland, the Ministry of Science, Education and Sports of the Republic of Croatia, RosAtom of Russia and German Bundesministerium für Bildung, Wissenschaft, Forschung und Technologie (BMBF), Helmholtz Association, Ministry of Education, Culture, Sports, Science, and Technology (MEXT) and Japan Society for the Promotion of Science (JSPS).

-
- [1] K. Fukushima and T. Hatsuda, Rept. Prog. Phys. **74**, 014001 (2011).
- [2] P. Braun-Munzinger and J. Wambach, Rev. Mod. Phys. **81**, 1031 (2009).
- [3] M. Asakawa and K. Yazaki, Nucl. Phys. A **504**, 668 (1989).
- [4] Y. Aoki, G. Endrodi, Z. Fodor, S. D. Katz, and K. K. Szabo, Nature **443**, 675 (2006).
- [5] S. Ejiri, Phys. Rev. **D78**, 074507 (2008).
- [6] E. S. Bowman and J. I. Kapusta, Phys. Rev. **C79**, 015202 (2009).
- [7] M. M. Aggarwal *et al.* (STAR collaboration), Phys. Rev. Lett. **105**, 022302 (2010).
- [8] L. Adamczyk *et al.* (STAR collaboration), Phys. Rev. Lett. **112**, 032302 (2014).
- [9] J. Adam *et al.* (STAR collaboration), Phys. Rev. Lett. **126**, 092301 (2021).
- [10] L. Adamczyk *et al.* (STAR collaboration), Phys. Rev. Lett. **113**, 092301 (2014).
- [11] L. Adamczyk *et al.* (STAR collaboration), Phys. Lett. B **785**, 551 (2018).
- [12] M. Abdallah *et al.* (STAR), Phys. Rev. C **104**, 024902 (2021).
- [13] M. A. Stephanov, K. Rajagopal, and E. V. Shuryak, Phys. Rev. **D60**, 114028 (1999).
- [14] M. Stephanov, Phys. Rev. Lett. **107**, 052301 (2011).
- [15] <https://drupal.star.bnl.gov/STAR/starnotes/public/sn0598>, BES-II white paper: STAR Note.
- [16] B. Friman, F. Karsch, K. Redlich, and V. Skokov, Eur. Phys. J. **C71**, 1694 (2011).
- [17] S. Borsanyi, Z. Fodor, J. N. Guenther, S. K. Katz, A. Pasztor, I. Portillo, C. Ratti, and K. K. Szabo, JHEP **10**, 205 (2018).
- [18] W.-j. Fu, X. Luo, J. M. Pawłowski, F. Rennecke, R. Wen, and S. Yin, Phys. Rev. D **104**, 094047 (2021).
- [19] A. Bazavov *et al.*, Phys. Rev. **D101**, 074502 (2020).
- [20] L. Adamczyk *et al.* (STAR collaboration), Phys. Rev. C **96**, 044904 (2017).
- [21] X. Luo and N. Xu, Nucl. Sci. Tech. **28**, 112 (2017).
- [22] P. Garg, D. K. Mishra, P. K. Netrakanti, B. Mohanty, A. K. Mohanty, B. K. Singh, and N. Xu, Phys. Lett. B **726**, 691 (2013).
- [23] M. Asakawa and M. Kitazawa, Prog. Part. Nucl. Phys. **90**, 299 (2016).
- [24] X. Luo, Phys. Rev. **C91**, 034907 (2015).
- [25] V. Skokov, B. Friman, and K. Redlich, Phys. Rev. **C88**, 034911 (2013).
- [26] T. Sugiura, T. Nonaka, and S. Esumi, Phys. Rev. **C100**, 044904 (2019).
- [27] A. Pandav, D. Mallick, and B. Mohanty, Nucl. Phys. A **991**, 121608 (2019).
- [28] M. Kitazawa and M. Asakawa, Phys. Rev. **C86**, 024904 (2012), [Erratum: Phys. Rev. **C86**, 069902(2012)].
- [29] A. Bzdak and V. Koch, Phys. Rev. **C86**, 044904 (2012).
- [30] T. Nonaka, T. Sugiura, S. Esumi, H. Masui, and X. Luo, Phys. Rev. **C94**, 034909 (2016).
- [31] A. Bzdak and V. Koch, Phys. Rev. **C91**, 027901 (2015).
- [32] X. Luo and T. Nonaka, Phys. Rev. **C99**, 044917 (2019).
- [33] M. Kitazawa, Phys. Rev. **C93**, 044911 (2016).
- [34] T. Nonaka, M. Kitazawa, and S. Esumi, Phys. Rev. **C95**, 064912 (2017).
- [35] A. Bzdak, R. Holzmann, and V. Koch, Phys. Rev. **C94**, 064907 (2016).
- [36] S. Esumi, K. Nakagawa, and T. Nonaka, Nucl. Instrum. Meth. A **987**, 164802 (2021).
- [37] T. Nonaka, M. Kitazawa, and S. Esumi, Nucl. Instrum. Meth. **A906**, 10 (2018).
- [38] R. Barlow, in *Advanced Statistical Techniques in Particle Physics. Proceedings, Conference, Durham, UK, March 18-22, 2002* (2002) pp. 134-144.
- [39] M. Bleicher *et al.*, J. Phys. G **25**, 1859 (1999).
- [40] Y. Ohnishi, M. Kitazawa, and M. Asakawa, Phys. Rev. C **94**, 044905 (2016).
- [41] A. Bzdak, V. Koch, and V. Skokov, Phys. Rev. C **87**, 014901 (2013).
- [42] P. Braun-Munzinger, A. Rustamov, and J. Stachel, Nucl. Phys. A **960**, 114 (2017).
- [43] V. Vovchenko and V. Koch, Phys. Rev. C **103**, 044903 (2021).
- [44] V. Vovchenko, V. Koch, and C. Shen, (2021), arXiv:2107.00163 [hep-ph].
- [45] P. Braun-Munzinger, B. Friman, K. Redlich, A. Rusta-

mov, and J. Stachel, Nucl. Phys. A **1008**, 122141 (2021).
 [46] D. K. Mishra and P. Garg, (2017), arXiv:1706.04012
 [nucl-th].

where $G(\theta)$ is the moment generating function, and $P(N)$ is the probability distribution function to find N particles [23]. Similarly, the r th-order cumulant, C_r , is defined as

$$C_r = \frac{\partial^r}{\partial \theta^r} K(\theta)|_{\theta=0}, \quad K(\theta) = \ln \sum_N e^{N\theta} P(N), \quad (2)$$

where $K(\theta)$ is the cumulant generating function. The r th-order cumulant is then calculated recursively from lower-order moments as

$$C_r = \mu_r - \sum_{m=1}^{r-1} \binom{r-1}{m-1} C_m \mu_{r-m}. \quad (3)$$

In experiments, the measured cumulants have to be corrected for detector efficiencies. The efficiency correction of the r th-order cumulant, C_r^{cor} is performed with the following formulas [32, 34]:

SUPPLEMENTAL MATERIAL

1. Cumulants and efficiency correction

The shape of the distribution is characterized by r th-order moments $\langle N^r \rangle$ which are defined as

$$\mu_r = \frac{\partial^r}{\partial \theta^r} G(\theta)|_{\theta=0}, \quad G(\theta) = \sum_N e^{N\theta} P(N), \quad (1)$$

$$C^{cor} = \langle q_{(1,1)} \rangle_c, \quad (4)$$

$$C_2^{cor} = \langle q_{(1,1)}^2 \rangle_c + \langle q_{(2,1)} \rangle_c - \langle q_{(2,2)} \rangle_c, \quad (5)$$

$$C_3^{cor} = \langle q_{(1,1)}^3 \rangle_c + 3\langle q_{(1,1)}q_{(2,1)} \rangle_c - 3\langle q_{(1,1)}q_{(2,2)} \rangle_c + \langle q_{(3,1)} \rangle_c - 3\langle q_{(3,2)} \rangle_c + 2\langle q_{(3,3)} \rangle_c, \quad (6)$$

$$\begin{aligned} C_4^{cor} = & \langle q_{(1,1)}^4 \rangle_c + 6\langle q_{(1,1)}^2q_{(2,1)} \rangle_c - 6\langle q_{(1,1)}^2q_{(2,2)} \rangle_c + 4\langle q_{(1,1)}q_{(3,1)} \rangle_c + 3\langle q_{(2,1)}^2 \rangle_c \\ & + 3\langle q_{(2,2)}^2 \rangle_c - 12\langle q_{(1,1)}q_{(3,2)} \rangle_c + 8\langle q_{(1,1)}q_{(3,3)} \rangle_c - 6\langle q_{(2,1)}q_{(2,2)} \rangle_c \\ & + \langle q_{(4,1)} \rangle_c - 7\langle q_{(4,2)} \rangle_c + 12\langle q_{(4,3)} \rangle_c - 6\langle q_{(4,4)} \rangle_c, \end{aligned} \quad (7)$$

$$\begin{aligned} C_5^{cor} = & \langle q_{(1,1)}^5 \rangle_c + 10\langle q_{(1,1)}^3q_{(2,1)} \rangle_c - 10\langle q_{(1,1)}^3q_{(2,2)} \rangle_c + 10\langle q_{(1,1)}^2q_{(3,1)} \rangle_c - 30\langle q_{(1,1)}^2q_{(3,2)} \rangle_c \\ & + 20\langle q_{(1,1)}^2q_{(3,3)} \rangle_c + 15\langle q_{(2,2)}^2q_{(1,1)} \rangle_c + 15\langle q_{(2,1)}^2q_{(1,1)} \rangle_c - 30\langle q_{(1,1)}q_{(2,1)}q_{(2,2)} \rangle_c \\ & + 5\langle q_{(1,1)}q_{(4,1)} \rangle_c - 35\langle q_{(1,1)}q_{(4,2)} \rangle_c + 60\langle q_{(1,1)}q_{(4,3)} \rangle_c - 30\langle q_{(1,1)}q_{(4,4)} \rangle_c \\ & + 10\langle q_{(2,1)}q_{(3,1)} \rangle_c - 30\langle q_{(2,1)}q_{(3,2)} \rangle_c + 20\langle q_{(2,1)}q_{(3,3)} \rangle_c \\ & - 10\langle q_{(2,2)}q_{(3,1)} \rangle_c + 30\langle q_{(2,2)}q_{(3,2)} \rangle_c - 20\langle q_{(2,2)}q_{(3,3)} \rangle_c \\ & + \langle q_{(5,1)} \rangle_c - 15\langle q_{(5,2)} \rangle_c + 50\langle q_{(5,3)} \rangle_c - 60\langle q_{(5,4)} \rangle_c + 24\langle q_{(5,5)} \rangle_c, \end{aligned} \quad (8)$$

$$\begin{aligned} C_6^{cor} = & \langle q_{(1,1)}^6 \rangle_c + 15\langle q_{(1,1)}^4q_{(2,1)} \rangle_c - 15\langle q_{(1,1)}^4q_{(2,2)} \rangle_c + 20\langle q_{(1,1)}^3q_{(3,1)} \rangle_c - 60\langle q_{(1,1)}^3q_{(3,2)} \rangle_c \\ & + 40\langle q_{(1,1)}^3q_{(3,3)} \rangle_c - 90\langle q_{(1,1)}^2q_{(2,2)}q_{(2,1)} \rangle_c + 45\langle q_{(1,1)}^2q_{(2,1)}^2 \rangle_c + 45\langle q_{(1,1)}^2q_{(2,2)}^2 \rangle_c \\ & + 15\langle q_{(2,1)}^3 \rangle_c - 15\langle q_{(2,2)}^3 \rangle_c + 15\langle q_{(1,1)}^2q_{(4,1)} \rangle_c - 105\langle q_{(1,1)}^2q_{(4,2)} \rangle_c + 180\langle q_{(1,1)}^2q_{(4,3)} \rangle_c - 90\langle q_{(1,1)}^2q_{(4,4)} \rangle_c \\ & - 45\langle q_{(2,1)}^2q_{(2,2)} \rangle_c + 45\langle q_{(2,2)}^2q_{(2,1)} \rangle_c + 60\langle q_{(1,1)}q_{(2,1)}q_{(3,1)} \rangle_c - 180\langle q_{(1,1)}q_{(2,1)}q_{(3,2)} \rangle_c \\ & + 120\langle q_{(1,1)}q_{(2,1)}q_{(3,3)} \rangle_c - 60\langle q_{(1,1)}q_{(2,2)}q_{(3,1)} \rangle_c + 180\langle q_{(1,1)}q_{(2,2)}q_{(3,2)} \rangle_c - 120\langle q_{(1,1)}q_{(2,2)}q_{(3,3)} \rangle_c \\ & + 6\langle q_{(1,1)}q_{(5,1)} \rangle_c - 90\langle q_{(1,1)}q_{(5,2)} \rangle_c + 300\langle q_{(1,1)}q_{(5,3)} \rangle_c - 360\langle q_{(1,1)}q_{(5,4)} \rangle_c + 144\langle q_{(1,1)}q_{(5,5)} \rangle_c \\ & + 15\langle q_{(2,1)}q_{(4,1)} \rangle_c - 105\langle q_{(2,1)}q_{(4,2)} \rangle_c + 180\langle q_{(2,1)}q_{(4,3)} \rangle_c - 90\langle q_{(2,1)}q_{(4,4)} \rangle_c \\ & - 15\langle q_{(2,2)}q_{(4,1)} \rangle_c + 105\langle q_{(2,2)}q_{(4,2)} \rangle_c - 180\langle q_{(2,2)}q_{(4,3)} \rangle_c + 90\langle q_{(2,2)}q_{(4,4)} \rangle_c \\ & + 10\langle q_{(3,1)}^2 \rangle_c - 60\langle q_{(3,1)}q_{(3,2)} \rangle_c + 40\langle q_{(3,1)}q_{(3,3)} \rangle_c + 90\langle q_{(3,2)}^2 \rangle_c - 120\langle q_{(3,2)}q_{(3,3)} \rangle_c + 40\langle q_{(3,3)}^2 \rangle_c \\ & + \langle q_{(6,1)} \rangle_c - 31\langle q_{(6,2)} \rangle_c + 180\langle q_{(6,3)} \rangle_c - 390\langle q_{(6,4)} \rangle_c + 360\langle q_{(6,5)} \rangle_c - 120\langle q_{(6,6)} \rangle_c, \end{aligned} \quad (9)$$

with

$$q_{(r,s)} = q_{(a^r/p^s)} = \sum_{i=1}^M (a_i^r/p_i^s) n_i, \quad (10)$$

where angle brackets represent represents a cumulant, M represents the number of efficiency bins, a_i and p_i represent the electric charge and efficiency at the i th efficiency bin, and r and s are the powers of a_i and p_i , respectively.

2. Efficiency distributions

In general, cumulants of net-particle distributions are corrected for detector efficiencies, and are assumed to follow binomial distributions [24, 28, 29, 34]. However, it was pointed out that the correction method loses its validity once the binomial assumption is broken [35, 37]. In order to check the efficiency distributions of the STAR detector, Monte-Carlo simulations are employed in the STAR detector environment. The number of reconstructed protons is used to study non-binomial effect of the detector in the most severe environment in terms of the particle multiplicity, MC tracks are embedded in the data for Au+Au 0-5% central collisions at $\sqrt{s_{\text{NN}}} = 200$ GeV. Efficiencies are also studied by varying the embedded number of protons and antiprotons to see the dependence of non-binomial effects on the track density.

Figure 4 shows reconstructed protons as black circles. Each panel represents a different number of embedded protons and antiprotons. Embedding data is then fitted by the binomial distribution as shown by red solid lines in Fig. 4. The χ^2/ndf values can be found in each panel. The ratio of the fitted function to the embedding data is shown in the lower panels. It is found that the tail of the distributions in panel (e), (f),... (k) in Fig. 4 deviates from binomial distributions. The beta-binomial distribution is employed to fit the embedding data in addition to the binomial distribution. The beta-binomial distribution is defined as

$$\beta(n : N, a, b) = \int_0^1 d\varepsilon \mathcal{B}(\varepsilon, a, b) B(n; \varepsilon, N), \quad (11)$$

with the beta distribution being

$$\mathcal{B}(\varepsilon; a, b) = \varepsilon^a (1 - \varepsilon)^b / B(a, b), \quad (12)$$

where $B(a, b)$ is the beta function. Each variable is defined through a model as follows. It is known that the beta-binomial distribution is given by an urn model. Let us consider N_w white balls and N_b black balls in the urn. One draws a ball from the urn. If it is white (black), return two white (black) balls to the urn. This procedure is repeated N times, then the resulting distribution of n (white balls) is given by the beta-binomial distributions as $\beta(n; N, N_w, N_b)$. This is equivalent to $\beta(n; N, \alpha, \varepsilon)$, where $N_w = \alpha N$ with $\varepsilon = N_w / (N_w + N_b)$. Smaller α gives a broader distribution than the binomial, while the distribution becomes close to the binomial distribution with larger α . The beta-binomial distributions are numerically generated using various values of α . They are compared to the embedding data to determine the best parameter α to fit the efficiency distributions.

The fitted function is shown by the green dotted lines in Fig. 4. The values of χ^2/ndf are found to be around unity in most of $(N_p, N_{\bar{p}})$. This indicates that the STAR efficiency follows the beta-binomial distribution in Au+Au

collisions 0-2.5% centrality at $\sqrt{s_{\text{NN}}} = 200$ GeV. Similar checks are done for 2.5-5.0% centrality. It is found that the efficiency distribution follows the beta-binomial distribution also for 2.5-5.0% centrality.

$(N_p, N_{\bar{p}})$	χ^2/ndf values	
	binomial	beta-binomial (α)
(10,10)	5.2	1.0 (22)
(10,20)	5.2	0.9 (22)
(10,40)	6.0	0.6 (15)
(20,5)	7.2	0.8 (12)
(20,10)	7.5	1.0 (10)
(20,20)	8.0	1.2 (10)
(20,40)	7.1	1.0 (11)
(40,5)	14.2	1.0 (6)
(40,10)	15.1	0.9 (5)
(40,20)	17.1	1.8 (6)
(40,40)	17.8	1.6 (6)

TABLE I. χ^2/ndf of fit results in Fig. 4 for the given combinations of embedded protons and antiprotons from embedding simulations in 200 GeV Au+Au collisions at 0-2.5% centrality. The non-binomial parameter α is also shown for results using the beta-binomial distribution.

3. Non-binomial efficiency correction

Two correction methods for non-binomial efficiency are employed. One is the unfolding approach to reconstruct the distribution itself [36], and the other one is the moment expansion to correct moments in an analytic way [37]. Both methods utilize knowledge of the detector response between generated and reconstructed particles computed by detector simulations, which is called response matrix. From the embedding simulation discussed in Sec. 2, ε and α are parameterized as a function of N_p and $N_{\bar{p}}$. Using the parametrization, the 4-dimensional response matrices between generated/reconstructed coordinates for protons and antiprotons are generated using 1 billion events. Another two response matrices are also generated using $\alpha - \sigma$ and $\alpha + \sigma$, where σ is the statistical uncertainty on α . Furthermore, the response matrices of the binomial distribution are generated with track density dependence of the efficiency implemented¹ [35]. Those response matrices are utilized to correct for the detector effects. We have checked that both the unfolding approach and the moment expansion method [36, 37] give consistent cumulant results. Thus, we focus on the results of the unfolding approach in the rest of this section.

It should be noted that in Ref. [9] the effect of non-binomial effects of up to the fourth-order cumulants and their ratios are discussed and found to be small within statistical uncertainties. Therefore, we present the effects

¹ The track density here represents event-by-event (anti)protons in the generated coordinate, which cannot be considered in the conventional efficiency correction method. Note that the dependence of efficiency on the total multiplicity is already taken into account in the centrality bin width correction (CBWC).

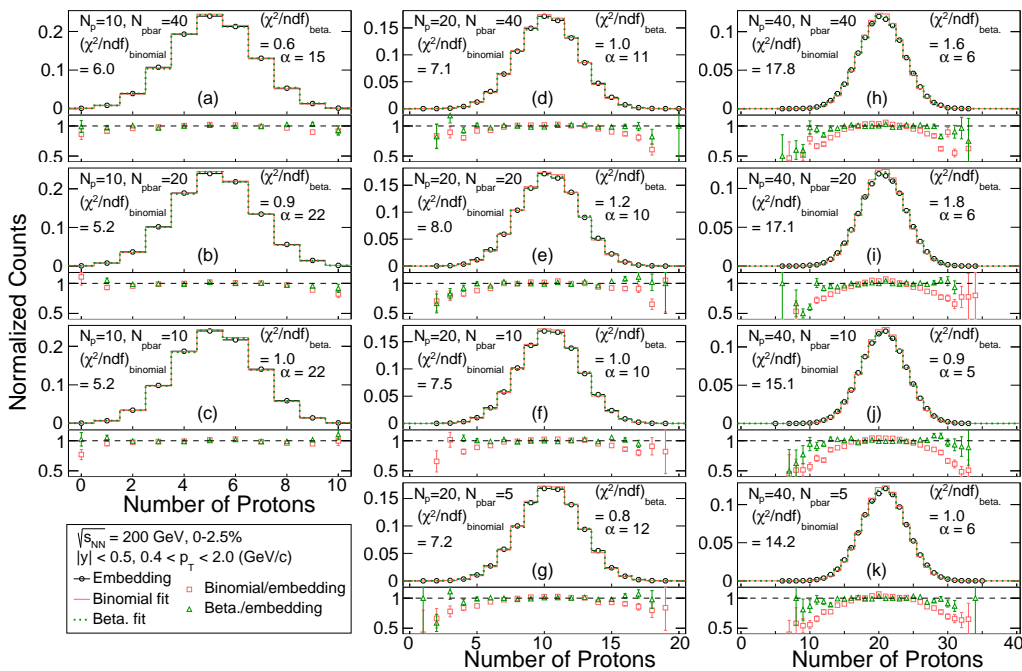


FIG. 4. Distributions of reconstructed protons (black circles) from embedding simulations in 200 GeV Au+Au collisions at 0-2.5% centrality. Red lines are fits with the binomial distribution, and green dotted lines represent the fit with the beta-binomial distributions using α that gives the minimal χ^2/ndf . Each panel shows the result from the given combinations of embedded protons and antiprotons. The ratio of fits to the embedding data is shown for each panel.

on the higher-order cumulants and ratios, $C_5, C_6, C_5/C_1$, and C_6/C_2 for Au+Au collisions at $\sqrt{s_{NN}} = 200$ GeV 0-5% centrality as shown in Fig. 5. For each column, the first two points are the results corrected for the binomial detector response, and last three points are from the unfolding with beta-binomial response using different non-binomial parameters. The dependence of efficiency on the track density (N_p and $N_{\bar{p}}$ themselves) is taken into account for the last four points. Those results are arbitrarily ordered from left to right as response matrices have larger deviations compared to the binomial distribution. They are calculated for 0-2.5% and 2.5-5.0% centralities separately and averaged to 0-5% centrality. Table II summarizes the cumulant ratios and their errors. Results corrected for beta-binomial response matrices with non-binomial parameters being $\alpha \pm \sigma$ are considered as systematic uncertainties. Statistical and systematic uncertainties are added in quadrature to calculate total uncertainties. The deviations of results corrected for non-binomial efficiencies compared to the binomial efficiency correction is found to be less than 1 sigma for C_5/C_1 and C_6/C_2 .

Again, we note that these results are from 200 GeV Au+Au collisions at 0-5% centrality. This is the highest Au+Au collision energy at RHIC, where the high multiplicity is expected to result in the largest non-binomial detector effects. It is noteworthy that the experimental data for 200 GeV has the largest statistics among the studied datasets. Therefore, we conclude that the non-binomial detector effects on higher-order cumulants and their ratios would be within errors for all BES-I energies.

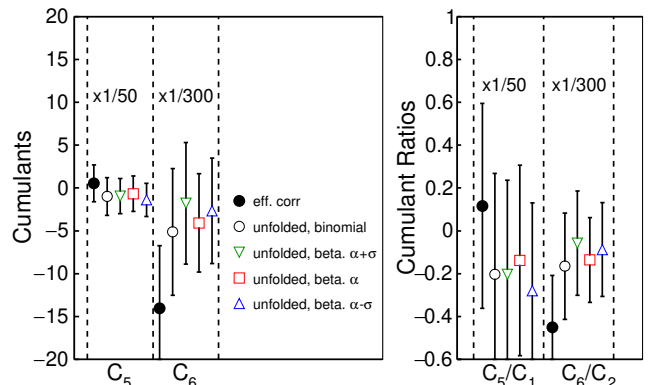


FIG. 5. Cumulants and their ratios up to the sixth order corrected for non-binomial efficiencies for 200 GeV Au+Au collisions at 0-5% centrality. The CBWC is applied for 2.5% centrality bin width. Results from the conventional efficiency correction are shown as black filled circles, results from the unfolding with the binomial detector response are shown as black open circles, and results from beta-binomial detector response with $\alpha + \sigma$, α and $\alpha - \sigma$ are shown in green triangles, red squares and blue triangles, respectively. $C_5, C_6, C_2/C_1, C_5/C_1$ and C_6/C_2 are scaled by constant shown in each column.

4. Effect of centrality bin width correction (CBWC)

Figure 6 shows centrality dependence of net-proton C_6/C_2 from Au+Au $\sqrt{s_{NN}} = 200$ GeV collisions. The centrality bin width correction (CBWC) [21] is applied for the red markers to suppress the effect from initial vol-

Cumulant ratio	binomial \pm stat.err	beta. \pm stat.err \pm sys.err	significance
C_2/C_1	$1.3 \pm 1.2 \times 10^{-3}$	$1.2 \pm 1.3 \times 10^{-3} \pm 3.1 \times 10^{-2}$	3.1
C_3/C_2	$0.13 \pm 1.2 \times 10^{-2}$	$0.13 \pm 1.2 \times 10^{-2} \pm 3.0 \times 10^{-3}$	4.7×10^{-2}
C_4/C_2	1.1 ± 0.21	$0.97 \pm 0.21 \pm 8.4 \times 10^{-2}$	4.2×10^{-1}
C_5/C_1	0.1 ± 0.48	$-0.14 \pm 0.44 \pm 0.11$	3.8×10^{-1}
C_6/C_2	-0.45 ± 0.24	$-0.14 \pm 0.20 \pm 6.5 \times 10^{-2}$	1.0

TABLE II. Cumulant ratios and their statistical errors (second column) from the conventional efficiency correction with the binomial detector response, and (third column) from unfolding with the beta-binomial detector response. Systematic errors are also shown for the beta-binomial case. The last column shows the difference between the two results normalized by the total errors mentioned above.

ume fluctuations. No volume correction is applied for the star markers. One can see that the volume fluctuations enhance the value of net-proton C_6/C_2 . Note that there is no perfect solution to remove the volume fluctuations, hence the data driven approach, CBWC, is employed in the measurements.

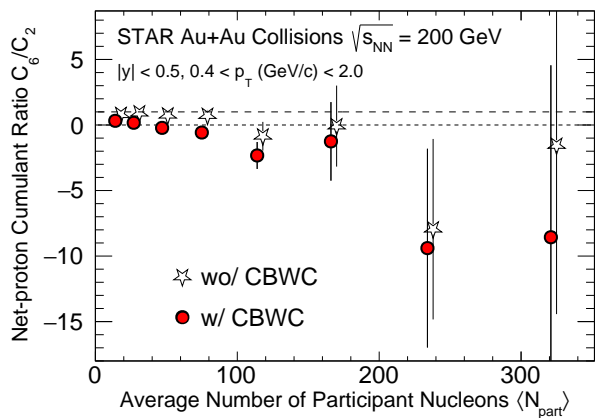


FIG. 6. Collision centrality dependence of net-proton C_6/C_2 in Au+Au collisions for $\sqrt{s_{NN}} = 200$ GeV within $|y| < 0.5$ and $0.4 < p_T$ (GeV/c) < 2.0 . Results with and without the CBWC are overlaid. The results are corrected for detector efficiencies. Points for different calculation methods are staggered horizontally to improve clarity.

5. UrQMD calculations

Figure 7 shows centrality dependence of net-proton C_6/C_2 from experimental data and UrQMD calculations

for $\sqrt{s_{NN}} = 27, 54.4, \text{ and } 200$ GeV. The UrQMD results are merged for 0-30%, 30-60%, and 60-80% centralities to reduce statistical uncertainties. One can see that the C_6/C_2 values from three collision energies in UrQMD calculations are consistent with each other within uncertainties, and therefore they are merged to reduce statistical fluctuations in the paper.

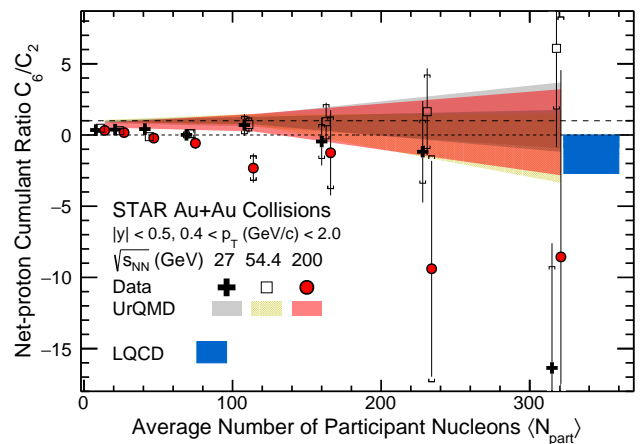


FIG. 7. Collision centrality dependence of net-proton C_6/C_2 in Au+Au collisions for $\sqrt{s_{NN}} = 27, 54.4, \text{ and } 200$ GeV within $|y| < 0.5$ and $0.4 < p_T$ (GeV/c) < 2.0 . Points for different beam energies are staggered horizontally to improve clarity. Shaded and hatched bands show the results from UrQMD model calculations. The lattice QCD calculations [17, 19] for $T = 160$ MeV and $\mu_B < 110$ MeV. are shown as a blue band at $\langle N_{part} \rangle \approx 340$.